Measuring *hhWW* coupling at lepton colliders

Qing-Hong Cao,[1,2,†] Kun Cheng,[1,‡] Yandong Liu,[3,4,*] and Xiao-Rui Wang[1,§]

[1]*School of Physics, Peking University, Beijing 100871, China*
[2]*Center for High Energy Physics, Peking University, Beijing 100871, China*
[3]*Key Laboratory of Beam Technology of Ministry of Education, College of Nuclear Science and Technology, Beijing Normal University, Beijing 100875, China*
[4]*Beijing Radiation Center, Beijing 100875, China*

(Received 25 December 2023; accepted 2 March 2024; published 8 April 2024)

The quartic Higgs-gauge-boson coupling g_{hhWW} is sensitive to the electroweak symmetry breaking mechanism; however, it is challenging to be measured at the Large Hadron Collider. We show that the coupling can be well probed at future lepton colliders through di-Higgs boson production via the vector boson fusion channel. We perform a detailed simulation of $\ell^+\ell^- \to \nu\bar{\nu}hh \to 4b + \not{E}_T$ with parton showering effects at e^+e^-, $\mu^+\mu^-$ and $e^-\mu^+$ colliders. We find that the regions of $g_{hhWW}/g^{\rm SM}_{hhWW} < 0.86$ and $g_{hhWW}/g^{\rm SM}_{hhWW} > 1.32$ can be discovered at the 5σ confidence level at the 10 TeV $\mu^+\mu^-$ collider with an integrated luminosity of 3 ab^{-1}. We also demonstare that $g_{hhWW}/g^{\rm SM}_{hhWW}$ is constrained within [0.72, 1.66], [0.72, 1.70], [0.84, 1.32], and [0.88, 1.14] at the 1 TeV e^+e^-, $e\mu$ colliders, 2 TeV $e\mu$ collider, and 10 TeV $\mu^+\mu^-$ collider, respectively, given null excess observed at the 2σ confidence level with an integrated luminosity of 3 ab^{-1}.

DOI: 10.1103/PhysRevD.109.073005

I. INTRODUCTION

The discovery of the Higgs boson [1,2] has significant implications for the study of its characteristics, including its mass, spin, and interactions with other particles in the Standard Model (SM). Yet, our understanding of the electroweak symmetry breaking (EWSB) mechanisms and the true character of the Higgs boson remains shrouded in mystery. The couplings of the Higgs boson to $W^\pm$ and Z bosons, g_{hVV} and g_{hhVV}, pivotal for insights into EWSB, are intrinsically linked to the interactions of the gauge interactions and pattern of EWSB. The SM values of the couplings, $g^{\rm SM}_{hVV}$ and $g^{\rm SM}_{hhVV}$, are uniquely fixed by the weak charge of the scalar doublet. The interrelationship of these couplings manifests the internal consistency of the SM and ensures perturbative unitarity of gauge boson scatterings.

These couplings, however, can be altered in new physics (NP) models. To describe the NP effects in these couplings, we define κ_{hhVV} and κ_{hVV} as

$$\kappa_{hhVV} \equiv \frac{g_{hhVV}}{g^{\rm SM}_{hhVV}}, \qquad \kappa_{hVV} \equiv \frac{g_{hVV}}{g^{\rm SM}_{hVV}}. \tag{1}$$

Any deviation of κ_{hhVV} and κ_{hVV} from unity implies the existence of NP. For instance, a singlet scalar extension model predicts that both the g_{hhVV} and g_{hVV} couplings will decrease compared to the SM due to mixings, leading to κ_{hhVV} and κ_{hVV} that are less than 1. Doublet scalar extension models might decrease g_{hVV}, but leave g_{hhVV} unchanged due to EWSB constraints. Consequently, in these models, κ_{hVV} is less than 1, but κ_{hhVV} retains the SM value. Furthermore, a larger $\kappa_{hVV/hhVV}$ is predicted in the scalar triplet or larger representations, owing to increasing Clebsch-Gordan coefficients. On the other hand, both the couplings g_{hVV} and g_{hhVV} are reduced in the Composite Higgs Model, in which the coupling ratio $\kappa_{hVV} = \sqrt{1-\xi}$ and $\kappa_{hhVV} = 1$–2ξ, where $\xi = v^2/f^2$, v is the electroweak symmetry breaking scale and f represents the compositeness scale [3].

Measuring κ_{hhVV} and κ_{hVV} and investigating their relation would shed light on the mechanism of EWSB. The ratio κ_{hVV} can be precisely pinned down by the vector boson fusion (VBF) type single Higgs production at the LHC [4,5] as κ_{hVV} can be extracted directly from $\kappa_{hVV} = \sqrt{\sigma_h/\sigma^{\rm SM}_h}$, where σ_h is the cross section of VBF-type single Higgs production and $\sigma^{\rm SM}_h$ is the SM prediction. However, it is difficult to measure the ratio κ_{hhVV} at the LHC, because κ_{hhVV} can only be measured from VBF type di-Higgs

*Corresponding author: ydliu@bnu.edu.cn
†qinghongcao@pku.edu.cn
‡chengkun@pku.edu.cn
§xiaorui_wong@pku.edu.cn

production processes while the gluon fusion processes is the dominant di-Higgs production processes at the LHC [6]. Presently, the LHC provides a loose constraint on κ_{hhVV} with $0 < \kappa_{hhVV} < 2.1$ [7,8]. At the high luminosity LHC, the κ_{hhVV} is anticipated to be measured with a precision of 40% by employing graph neural network techniques [9].

In our study, we investigate the VBF-type di-Higgs production at future high-energy lepton colliders [10–12], and we focus on the measurement of Higgs-gauge-boson couplings. The rest of this paper is organized as follows. The cross section of different di-Higgs production is described in Sec. II. The selection and reconstruction of events is presented in Sec. III, and the result is shown in Sec. IV. Finally we conclude in Sec. V.

II. DI-HIGGS PRODUCTION CROSS SECTION AT FUTURE LEPTON COLLIDERS

At high-energy lepton colliders, di-Higgs boson production can be instigated through several processes, including the VBF process, the Z-boson associated production (Zhh) process, and the loop-induced hh pair production process. Figure 1 plots the cross section for each process as a function of the collision energy $\sqrt{s}$. The contribution of the loop-induced process is very small due to the loop suppression, and the s-channel production cross section of Zhh decreases with collision energy when $\sqrt{s}$ exceeds 1 TeV due to s-channel suppression. Contrarily, the VBF production cross section increases with $\log \sqrt{s}/m_V$, as the collinear splitting mechanism of the electroweak gauge bosons becomes the dominant phenomena of the initial state radiation at high energy [13]. Besides, the cross section of the charged current process (mediated by $W^{\pm}$) is approximately an order of magnitude larger than that of the neutral current process (mediated by Z). Therefore, we mainly focus on the $W^{\pm}$ fusion process in the subsequent analysis.

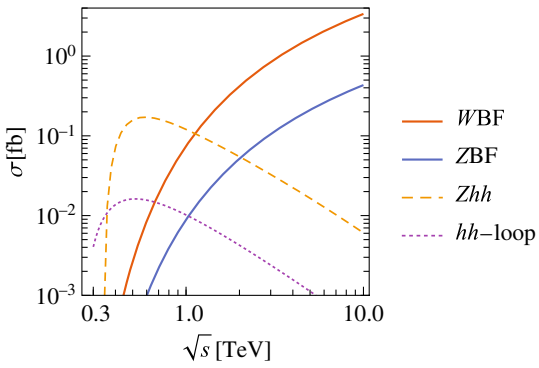

FIG. 1. The cross sections of di-Higgs boson production at lepton colliders as a function of colliding energies ($\sqrt{s}$), where WBF and ZBF stand for the VBF process mediated by the W and Z boson, respectively.

The VBF type di-Higgs production involves both the couplings g_{hWW} and g_{hhWW}; see Fig. 2. Therefore, measuring g_{hhWW} via di-Higgs production also relies on the value of g_{hWW}. Fortunately, the ratio κ_{hWW} can be precisely measured from single Higgs production via the VBF process and Vh associated process. Combining both the single and di-Higgs production, one can determine the κ_{hhWW}. In Fig. 3, we plot the contours of κ_{hhWW} in the plane of $\sigma_h/\sigma_h^{\mathrm{SM}}$ and $\sigma_{hh}/\sigma_{hh}^{\mathrm{SM}}$. Even though a degeneracy of κ_{hhWW} appears for given total cross sections σ_h and σ_{hh}, it can be resolved by analyzing the m_{hh} distribution. In the work we performed simulations at three kinds of lepton colliders:

(1) e^+e^- collider with collision energy of $\sqrt{s} = 1$ TeV,
(2) $e\mu$ collider with collision energies of $\sqrt{s} = 1$ TeV and $\sqrt{s} = 2$ TeV [14],
(3) $\mu^+\mu^-$ collider with collision energy of $\sqrt{s} = 10$ TeV [15].

Assuming the SM value of trilinear Higgs boson self-coupling, the coupling dependence of the cross section can be parametrized as

$$\sigma^{hh} = \kappa_{hhWW}^2\sigma_a + \kappa_{hWW}^4\sigma_b + \kappa_{hWW}^2\sigma_c + \kappa_{hhWW}\kappa_{hWW}^2\sigma_{ab} + \kappa_{hWW}^3\sigma_{bc} + \kappa_{hhWW}\kappa_{hWW}\sigma_{ac}, \quad (2)$$

where σ_a, σ_b and σ_c parametrize the contribution from the Feynman diagram (a), (b), and (c) in Fig. 2, respectively; σ_{ab}, σ_{ac}, and σ_{bc} denote the interference between each Feynman diagram. For the process of $l^-l^+ \to \nu_l\bar{\nu}_l hh$, the contribution from each Feynman diagram and their interference effects are shown in Fig. 4, and we also show the values with the benchmark collision energies in Table I.

When the ratio κ_{hhWW} has a deviation from its SM value with $\delta\kappa_{hhWW}$, namely $\kappa_{hhWW} = 1 + \delta\kappa_{hhWW}$, the leading contribution of the deviation arises from diagram (a) and its interference between other diagrams; see Eq. (2). It is observed in Fig. 4 that σ_a, σ_b, and σ_{ab} increase with collision energy and dominate at high energy. Therefore, the cross section becomes more sensitive to κ_{hhWW} with a larger collision energy. The underlying physics of this explosion of σ_a, σ_b and σ_{ab} with respect to the energy is the violation of perturbative unitarity; see Appendix for details. Therefore, the high energy lepton colliders are ideal to test NP models that change the Higgs-gauge-boson coupling g_{hhWW}.

III. COLLIDER SIMULATION

We consider three lepton colliders, the e^+e^- collider and $\mu^+\mu^-$ collider with symmetric incident beam energies, and the $e\mu$ collider with asymmetric incident beams, and we explore their potential of measuring the κ_{hhWW} coupling through the VBF-type di-Higgs production. Owing to the clean environment of the lepton colliders, one can reconstruct the two Higgs bosons in the $b\bar{b}$ decay mode, the

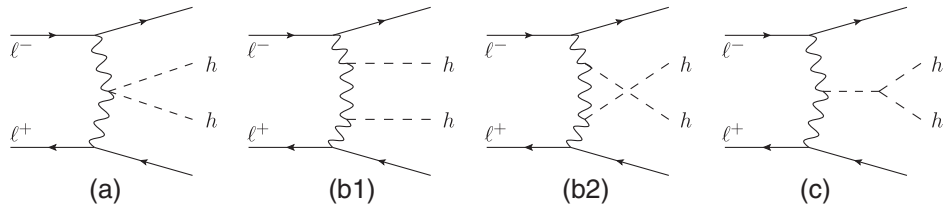

FIG. 2. Feynman diagrams of the di-Higgs boson production via VBF processes at lepton colliders.

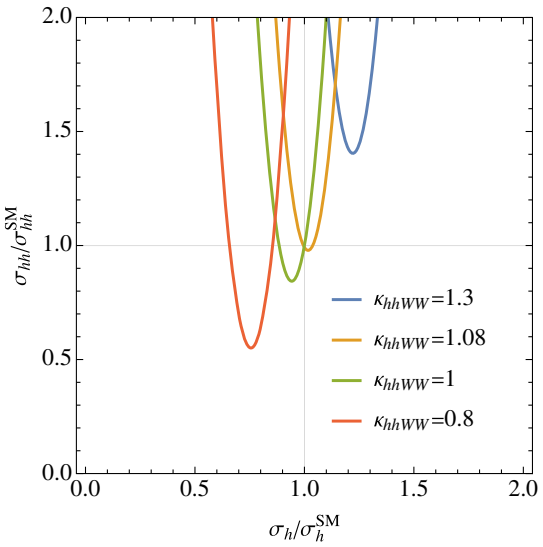

FIG. 3. Contours of κ_{hhWW} in the plane of $\sigma_h/\sigma_h^{\rm SM}$ and $\sigma_{hh}/\sigma_{hh}^{\rm SM}$, where σ_h and σ_{hh} present the cross section of the VBF type single-Higgs boson production and the di-Higgs boson production at the 10 TeV muon collider, respectively. The value of κ_{hWW} varies in each contour line of κ_{hhWW}, and the values of κ_{hWW} and κ_{hhWW} can be pinned down with a precision measurement of both the cross sections σ_h and σ_{hh}.

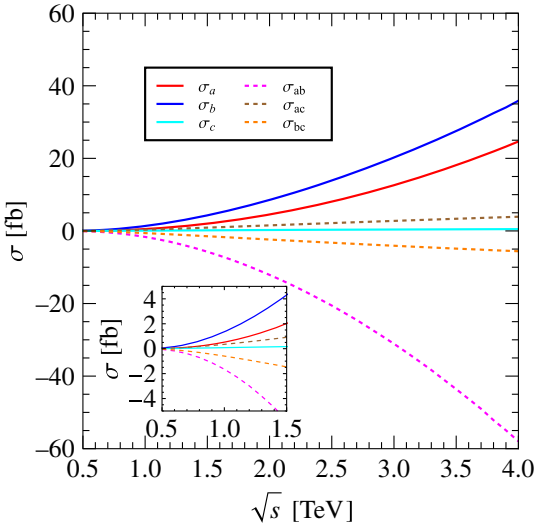

FIG. 4. Cross section of the W-boson fusion process $\ell^+\ell^- \to \bar{\nu}_\ell \nu_\ell hh$ from the contribution of each diagram and their interferences.

mode with the largest branching ratio. This leads to a distinct signature comprising four b jets and missing energy $\not{E}_T$ from two invisible neutrinos, in all the three lepton colliders.

The primary background processes for the $4b + \not{E}_T$ signal are $\ell_i^-\ell_j^+ \to \nu_i\bar{\nu}_j b\bar{b}b\bar{b}$ from the on-shell hZ/ZZ production, and $\ell^\pm\gamma \to b\bar{b}jj\nu\ell(\bar{\nu}\ell)$ from the on shell $hW^\pm/ZW^\pm$ production [10]. In addition, the $\ell^+\ell^- \to b\bar{b}b\bar{b}$ process, arising from the on shell Zh or ZZ production, may also contribute to the background at the e^+e^- collider and $\mu^+\mu^-$ collider, where $\not{E}_T$ is mimicked by undetected particles in the showering. Nevertheless, the reducible $4b$ backgrounds can be effectively suppressed by employing a relatively large $\not{E}_T$ cut or a recoil mass cut, as discussed below.

A. Symmetric e^+e^- and $\mu^+\mu^-$ colliders

First, we focus on the symmetric colliders, namely the e^+e^- and $\mu^+\mu^-$ colliders. The e^+e^- collider is proposed as a precision machine that benefits from the clear collision environment [16–19]. The $\mu^+\mu^-$ collider, as proposed in [20–22], offers not only a clean environment but also a high collision energy [23–28]. While technical difficulties [29,30] arise from the short lifetime, they can be compensated for by the advantage of increasing instantaneous luminosity with beam energy [30]. We use the e^+e^- collider with $\sqrt{s} = 1$ TeV and the $\mu^+\mu^-$ collider with $\sqrt{s} = 10$ TeV as examples in our analysis.

In the following simulation, we generate parton-level events using MadEvent [31], and then pass them to PYTHIA8 [32] for showering and hadronization. The showered events are clustered using FASTJET [33] using an anti-k_T algorithm with clustering parameter $\Delta R = 0.5$, and we subsequently simulate collider effects with DELPHES [34]. We adopt the tracking and energy resolution modeling used

TABLE I. Parametrization of parton level cross sections of $l^-l^+ \to \nu_l\bar{\nu}_l hh$ at lepton colliders.

Cross section [fb]	σ_a	σ_b	σ_c	σ_{ab}	σ_{bc}	σ_{ac}
1 TeV e^+e^- collider	0.54	1.41	0.09	−1.69	−0.62	0.35
1 TeV $e\mu$ collider	0.54	1.41	0.09	−1.69	−0.62	0.35
2 TeV $e\mu$ collider	4.80	9.02	0.34	−12.72	−2.53	1.53
10 TeV $\mu^+\mu^-$ collider	177.2	206.1	0.88	−378.10	−12.11	9.08

in DELPHES as specified in [18]. We select a benchmark b jet (mis-)tagging efficiencies from Ref. [18] with the higher identification rate,

$$p_{b\to b} = 0.9, \qquad p_{c\to b} = 0.3, \qquad p_{j\to b} = 0.05, \quad (3)$$

where j represents gluon or light quarks.

For the preselection, we require both the signal and backgrounds to satisfy the following cuts:

$$n^{\ell}(p_T > 10\ \text{GeV}) = 0, \qquad \not{E}_T > 10\ \text{GeV},$$
$$p_T^{\text{jet}} > 15\ \text{GeV}, \qquad -4.0 < \eta^{\text{jet}} < 4.0, \qquad \Delta R^{mn} > 0.5, \quad (4)$$

where ℓ denotes an electron or muon, $m(n)$ represents a reconstructed lepton or jet, and ΔR is the rapidity and azimuthal distance defined as $\Delta R^{mn} = \sqrt{\Delta\eta_{mn}^2 + \Delta\phi_{mn}^2}$. To eliminate backgrounds mediated by neutral current interactions, we require a $\not{E}_T$ signal and no isolated leptons with transverse momenta larger than 10 GeV. To effectively reconstruct the two Higgs bosons, we require at least four b jets and divide the four leading ones into two pairs by minimizing $\chi^2_{ijkl} = (m_{b_ib_j} - m_h)^2 + (m_{b_kb_l} - m_h)^2$. The two pairs of b jets are treated as two Higgs boson candidates. Then we impose the requirement that the invariant mass of the two b jets in each pair must satisfy

$$100\ \text{GeV} < m_{bb} < 150\ \text{GeV}, \quad (5)$$

which enhances signal-to-backgrounds ratio dramatically; see Tables II and III.

To further suppress electroweak resonance backgrounds, we require the likelihood of the four b jets originating from the Higgs boson pair to be larger than that from a ZZ pair or Zh pair. We achieve this by employing the function $\chi^2(m_1, m_2)$, defined as

$$\chi^2(m_1, m_2) \equiv \min_{i,j,k,l}\left[(m_{b_ib_j} - m_1)^2 + (m_{b_kb_l} - m_2)^2\right], \quad (6)$$

which represents the minimal mass difference between two b jet pairs and $m_{1(2)}$. We then require the four leading b jets in each event to satisfy

$$\text{HHCUT}: \chi^2(m_h, m_h) < \chi^2(m_Z, m_Z), \chi^2(m_h, m_h) < \chi^2(m_h, m_Z). \quad (7)$$

The selection criteria employed in this study effectively reduces the $ZZ + \not{E}_T$ and $Zh + \not{E}_T$ backgrounds and preserves the signal cross section, as illustrated in the fourth columns of Tables II and III.

At last, the process $e^+e^- \to b\bar{b}b\bar{b}$ stemming from Zh/ZZ resonant production often presents a non-negligible background. For example, at the 1 TeV e^+e^- collider, the cross section of these two nonintrinsic backgrounds is still larger than the signal cross section after imposing all the previous cuts. Although it is feasible to reject these backgrounds by increasing the $\not{E}_T$ cut in Eq. (4), this approach also reduces signal events considerably. A more effective strategy is to impose a cut on the recoil mass, defined as

$$M_{\text{recoil}} \equiv \sqrt{(p_1 + p_2 - p_{h_1} - p_{h_2})^2}, \quad (8)$$

where p_1 and p_2 represent the momenta of initial lepton, and p_{h_1} and p_{h_2} denote the momenta of reconstructed

TABLE II. Cut flow for the SM $\nu\bar{\nu}hh$ di-Higgs signal and background cross sections at the 1 TeV electron-positron collider (left) and 10 TeV muon collider (right).

σ [ab]	Precuts	m_{bb} cut	HHCUT	M_{recoil} cut
Signal	15.9	9.7	8.3	5.7
$\nu\nu hZ$	54.4	11.1	6.3	5.5
$\nu\nu ZZ$	73.7	9.1	3.1	2.9
$\nu W^{\pm}h$	45.2	3.9	2.3	2.3
$\nu W^{\pm}Z$	47.0	2.5	1.1	1.1
Background	⋯	⋯	⋯	11.8

σ [ab]	Precuts	m_{bb} cut	HHCUT	M_{recoil} cut
Signal	484.4	261.5	226.5	226.3
$\nu\nu hZ$	1163.1	168.6	97.8	97.6
$\nu\nu ZZ$	1557.9	121.2	36.7	36.6
$\nu W^{\pm}h$	560.7	26.2	17.2	17.2
$\nu W^{\pm}Z$	492.3	12.3	9.3	9.3
Background	⋯	⋯	⋯	160.7

TABLE III. Cut flow for the SM $\nu_e\bar{\nu}_\mu hh$ di-Higgs signal and background cross sections at the $e\mu$ collider with $E_e = 100$ GeV, $E_\mu = 2.5$ TeV (left) and $E_e = 170$ GeV, $E_\mu = 6$ TeV (right).

σ [ab]	Precuts	m_{bb} cut	HHCUT
Signal	12.2	6.8	5.5
$\nu\nu hZ$	49.8	9.3	5.2
$\nu\nu ZZ$	66.1	8.3	2.8
$\nu W^{\pm}h$	36.8	2.8	1.4
$\nu W^{\pm}Z$	40.2	2.2	0.9
Background	⋯	⋯	10.4

σ [ab]	Precuts	m_{bb} cut	HHCUT
Signal	69.9	37.6	31.5
$\nu\nu hZ$	205.5	33.1	19.3
$\nu\nu ZZ$	298.1	30.6	10.4
$\nu W^{\pm}h$	143.6	9.9	6.6
$\nu W^{\pm}Z$	139.6	6.5	2.8
Background	⋯	⋯	39.1

Higgs boson. We require a hard cut on M_{recoil}:

$$M_{\text{recoil}} \geq 200 \text{ GeV}, \tag{9}$$

as the two neutrinos in the signal tend to fly back-to-back and lead to a large recoil mass. We find that, after the M_{recoil} cut, the nonintrinsic backgrounds are negligible, and the signal cross section almost remains the same; see Table II. With an integrated luminosity of $3ab^{-1}$, the signal strength of the total cross section of di-Higgs production, $\mu_{hh} = \sigma_{hh}/\sigma_{hh}^{\text{SM}}$, can be constrained to $0.35 < \mu_{hh} < 1.80$ at the 1 TeV e^+e^- collider and $0.9 < \mu_{hh} < 1.1$ at the 10 TeV $\mu^+\mu^-$ collider, at 95% confidence level.

B. Asymmetric colliders

The electron-muon ($e\mu$) collider, initially proposed in Refs. [35–37], has drawn attention recently [14]. As a hybrid option, it is often considered to benefit from both the clean environment of electron colliders and the high beam energy of muon colliders. In this work, we use two benchmark colliding energies to illustrate the potential of the $e\mu$ collider for Higgs coupling measurements:

(1) A conventional 1 TeV setup with $E_e = 100$ GeV and $E_\mu = 3$ TeV,
(2) A maximal colliding energy of 2 TeV with $E_e = 170$ GeV and $E_\mu = 6$ TeV.

The di-Higgs signal at the $e\mu$ collider is $4b + \not{E}_T$, similar to that at the e^+e^- collider, and the background processes are also comparable with the e^+e^- collider and the $\mu^+\mu^-$ collider. However, owing to nonzero lepton numbers in the initial state, the $e\mu$ collider is free from the SM s-channel backgrounds. Besides, there are no backgrounds from ZZ/Zh production at the $e\mu$ collider, and no need for a recoil mass cut. The collider simulation is similar to that of the e^+e^- collider. The calorimeter coverage range of the detector is set as $-4 < \eta < 6$ to simulate the energy asymmetric behavior of the $e\mu$ collider, where η is the rapidity of the final state objects. The following preselection cuts (precuts) are applied:

$$\begin{aligned} &n^{\ell}(p_T > 10 \text{ GeV}) = 0, \qquad \not{E}_T > 10 \text{ GeV}, \\ &p_T^{\text{jet}} > 15 \text{ GeV}, \qquad -3.0 < \eta^{\text{jet}} < 5.0, \qquad \Delta R^{mn} > 0.5. \end{aligned} \tag{10}$$

We then apply the same invariant mass cut and HHCUT as used for the symmetric colliders, with the cut flows of signal and background cross sections displayed in Table III. With an integrated luminosity of 3 ab^{-1}, the signal strength of the total cross section for di-Higgs production, $\mu_{hh} = \sigma_{hh}/\sigma_{hh}^{\text{SM}}$, can be constrained to $0.38 < \mu_{hh} < 1.78$ at the 1 TeV $e\mu$ collider and $0.75 < \mu_{hh} < 1.25$ at the 2 TeV $e\mu$ collider at 95% confidence level.

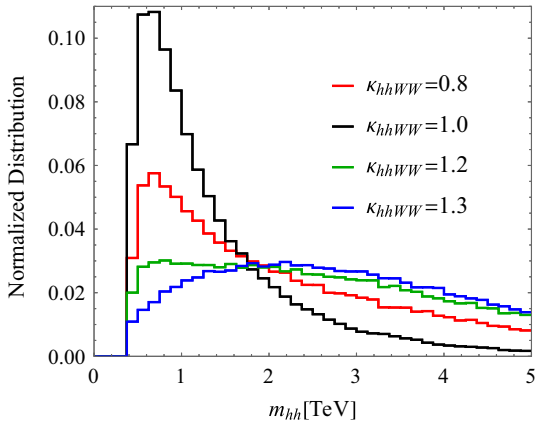

FIG. 5. Normalized m_{hh} distribution at 10 TeV $\mu^+\mu^-$ collider for different κ_{hhWW}, assuming κ_h and κ_{hWW} to be the SM value.

IV. ANALYSIS

Equipped with the simulation results, we explore the discovery potential of lepton colliders on Higgs-gauge coupling, equivalently, κ_{hhWW} and κ_{hWW}. As stated before, to measure κ_{hhWW} from the di-Higgs production, the κ_{hWW} must first be measured from the single Higgs production. However, with a fixed value of κ_{hWW}, the total di-Higgs cross section is a quadratic function of κ_{hhWW}; see Eq. (2). Therefore, the measurement of κ_{hhWW} may exhibit degeneracy. The degeneracy can be resolved by analyzing the m_{hh} distribution. As shown in Fig. 5, the m_{hh} distribution for different κ_{hhWW} is significantly different, which is a consequence of the unitarity violation when $\kappa_{hhWW} \neq 1$; see Appendix for details.

In the following, we perform a binned analysis which utilizes the information of m_{hh} distribution. The likelihood function for a Poisson distribution is given by

$$L(\vec{\kappa}) = \frac{(n_{\text{th}}(\vec{\kappa}))^{n_{\text{obs}}} e^{-n_{\text{th}}(\vec{\kappa})}}{n_{\text{obs}}!}, \tag{11}$$

where $\vec{\kappa} = (\kappa_{hWW}, \kappa_{hhWW})$ stands for the parameters in the theory, $n_{\text{th}}(\vec{\kappa})$ is the events number predicted by the theory, and n_{obs} is the observed events number. For the di-Higgs boson production, the events number from theory prediction is $n_{\text{th}}(\vec{\kappa}) = [\sigma_{hh}(\vec{\kappa}) + \sigma_{\text{bkg}}]\mathcal{L}$ with an integrated luminosity of $\mathcal{L}$, where σ_{hh} is the di-Higgs production cross section after applying selection cuts and σ_{bkg} is corresponding backgrounds. The logarithm of likelihood function can be defined as

$$-2\ln\lambda(\vec{\kappa}_1|\vec{\kappa}_0) = -2\ln\frac{L(\vec{\kappa}_1)}{L(\vec{\kappa}_0)}, \tag{12}$$

which depicts that the hypothesis $\vec{\kappa}_1$ is excluded versus $\vec{\kappa}_0$ with $\sqrt{-2\ln\lambda(\vec{\kappa}_1|\vec{\kappa}_0)}\sigma$ confidence level. For binned events, the likelihood function in Eq. (11) is modified as

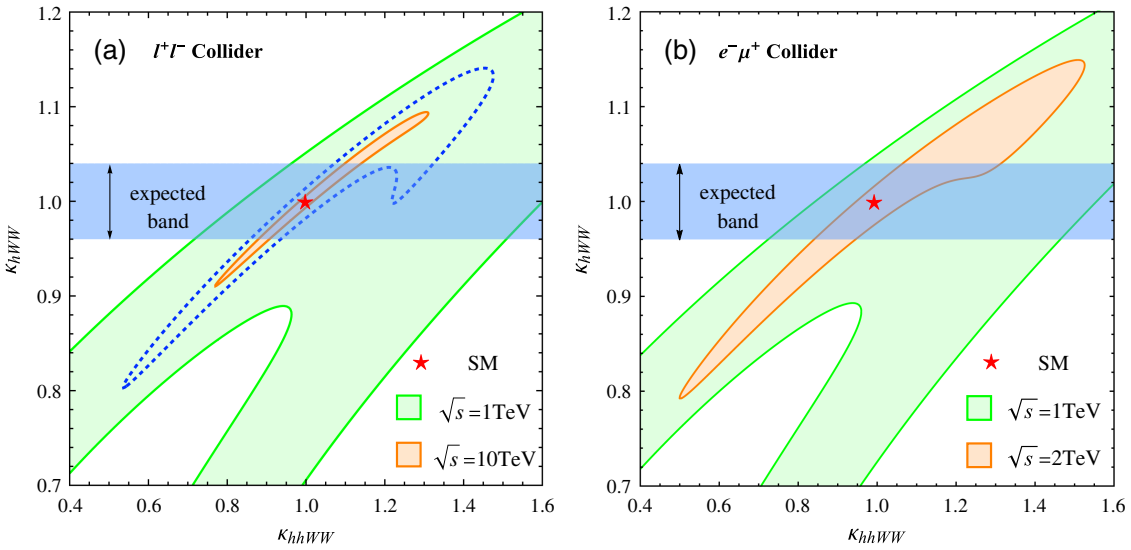

FIG. 6. Parameter space of κ_{hWW} and κ_{hhWW} that is consistent with SM ($\kappa_{hWW} = \kappa_{hhWW} = 1$) at 95% C.L. The left panel gives the results from the 1 TeV e^+e^- collider and 10 TeV $\mu^+\mu^-$ collider; the right panel is the case of the $e\mu$ collider with $\sqrt{s} = 1, 2$ TeV. The dashed contour in the left panel stands for the discovery capability at the 10 TeV $\mu^+\mu^-$ collider. The integrated luminosity is chosen as 3 ab^{-1}.

$$L(\vec{\kappa}) = \prod_i^N \frac{(n^i_{\rm th}(\vec{\kappa}))^{n^i_{\rm obs}} e^{-n^i_{\rm th}(\vec{\kappa})}}{n^i_{\rm obs}!}, \tag{13}$$

where $n^i_{\rm th}(\vec{\kappa})$ and $n^i_{\rm obs}$ are the theory predicted and observed event numbers in the ith bin.

With the likelihood presented above, we discern the potential for measuring Higgs-gauge-boson couplings. With an integrated luminosity of 3 ab^{-1}, the region of $-2\ln\lambda(\vec{\kappa}|\vec{\kappa}_{\rm SM}) \le 4$ is depicted in Fig. 6, where the observed number of events is assumed to be the SM prediction, i.e., $n^{(i)}_{\rm obs} = n^{(i)}_{\rm th}(\vec{\kappa}_{\rm SM})$. Figure 6(a) displays results from the e^+e^- collider and the $\mu^+\mu^-$ collider. The green region represents the $\kappa_{hhWW} - \kappa_{hWW}$ parameter space that is consistent with the SM at 95% C.L. at the 1 TeV e^+e^- collider, while the orange region denotes the same for the 10 TeV $\mu^+\mu^-$ collider. The red star marks the SM prediction where $\kappa_{hWW} = \kappa_{hhWW} = 1$. The dashed contour in Fig. 6(a) stands for the 5σ discovery capability at the 10 TeV $\mu^+\mu^-$ collider, i.e., the contour of $-2\ln\lambda(\vec{\kappa}_{\rm SM}|\vec{\kappa}) = 25$ where $n^{(i)}_{\rm obs}$ is assumed to be $n^{(i)}_{\rm th}(\vec{\kappa})$. The blue band denotes the 95% C.L. expected constraint on κ_{hWW} from the future electron-proton collider, namely $0.96 < \kappa_{hWW} < 1.04$ [5], while the current limit on κ_{hWW} at the 13 TeV LHC is $0.93 < \kappa_{hWW} < 1.22$ [4]. Figure 6(b) presents results from the asymmetric colliders, specifically the $e\mu$ collider with $\sqrt{s} = 1$ TeV (the green region) and $\sqrt{s} = 2$ TeV (the orange region).

From these figures, it is evident that the measurements become more accurate with increasing collision energy due to the rise in event numbers with $\sqrt{s}$, regardless of symmetric or asymmetric colliders. For example, in the e^+e^- collider and $e\mu$ collider with $\sqrt{s} = 1$ TeV, the signal and background event numbers are similar, as seen in Table III. Consequently, it is expected that the potentials are comparable, as shown by the green range in Fig. 6(a) and (b).

As shown in Fig. 6, with the expected limit on κ_{hWW}, we obtained the expected discovery sensitivity on κ_{hhWW}:

(1) 5σ discovery region $\kappa_{hhWW} < 0.86$ or $\kappa_{hhWW} > 1.32$ at the 10 TeV $\mu^+\mu^-$ collider,
(2) 2σ exclusion region $\kappa_{hhWW} < 0.88$ or $\kappa_{hhWW} > 1.14$ at the 10 TeV $\mu^+\mu^-$ collider,
(3) 2σ exclusion region $\kappa_{hhWW} < 0.72$ or $\kappa_{hhWW} > 1.70$ at the 1 TeV e^+e^- collider,
(4) 2σ exclusion region $\kappa_{hhWW} < 0.72$ or $\kappa_{hhWW} > 1.66$ at the 1 TeV $e\mu$ collider,
(5) 2σ exclusion region $\kappa_{hhWW} < 0.84$ or $\kappa_{hhWW} > 1.32$ at the 2 TeV $e\mu$ collider.

V. CONCLUSION

The quartic Higgs-gauge-boson coupling g_{hhVV} is essential to the electroweak symmetry breaking mechanism and gauge boson mass generation, and it can be measured in the VBF-type di-Higgs production. However, at hadron colliders, the process is typically overshadowed by the gluon-fusion di-Higgs production, making the extraction of g_{hhVV} challenging. In contrast, lepton colliders offer an ideal platform for probing the VBF-type di-Higgs production.

In the work we explored the potential of a lepton collider on the quartic Higgs-gauge-boson coupling, or equivalently, its ratio to SM prediction κ_{hhWW}. Detailed collider

simulations including parton showering effects were performed at the symmetric e^+e^- collider, $\mu^+\mu^-$ collider, and the asymmetric $e\mu$ collider. We found that the collider's potential to constrain κ_{hhWW} primarily depends on the collision energy. With an integrated luminosity of 3 ab^{-1}, the 2σ exclusion region is $\kappa_{hhWW} < 0.72$ or $\kappa_{hhWW} > 1.70$ and $\kappa_{hhWW} < 0.72$ or $\kappa_{hhWW} > 1.66$ at the 1 TeV e^+e^- collider and $e\mu$ collider ($E_e = 100$ GeV, $E_\mu = 3$ TeV), respectively. At the 2 TeV $e\mu$ collider ($E_e = 170$ GeV, $E_\mu = 6$ TeV), the 2σ exclusion region is $\kappa_{hhWW} < 0.84$ or $\kappa_{hhWW} > 1.32$, and it is $\kappa_{hhWW} < 0.88$ or $\kappa_{hhWW} > 1.14$ at 10 TeV $\mu^+\mu^-$ collider. In addition we obtain the 5σ discovery region of $\kappa_{hhWW} < 0.86$ or $\kappa_{hhWW} > 1.32$ at the 10 TeV $\mu^+\mu^-$ collider.

Note added. Near the completion of this work, Ref. [38] appeared with related content.

ACKNOWLEDGMENTS

The work of Q. H. C., K. C., and X. R. W. is partly supported by the National Science Foundation of China under Grants No. 11725520 and No. 12235001. The work of Y. D. L. is partly supported by the National Science Foundation of China under Grant No. 12075257.

APPENDIX: PERTURBATIVE UNITARITY

The nature of the VBF process can be ascertained by the factorized subprocess of $W^-W^+ \to hh$ in high energy collisions [39,40]. This is executed through the effective-W approximation method [41], and the cross section is expressed as the equation below:

$$\sigma(\ell^-\ell^+ \to \nu_\ell \bar{\nu}_\ell hh) = \sum_{i,j} \int dx_1 dx_2 P^i_{W^-/\ell^-}(x_1) P^j_{W^+/\ell^+} \times (x_2)\sigma\big(W_i^- W_j^+ \to hh\big). \tag{A1}$$

Here $P^i_{W^-/\ell^-}(x_1)$ denotes the gauge boson W^-'s probability distribution with polarization i in the electron; $x_1 = (E_{\ell^-} - E_{\nu_\ell})/E_{\ell^-}$ is the energy fraction of ℓ^- carried by W^-. The splitting functions for the collinear radiation of real W boson at leading order are [42]

$$\begin{aligned} P^+_{W/\ell}(x) &= \frac{g^2}{32\pi^2 x}\ln\left(\frac{4x^2E_\ell^2}{M_W^2}\right), \\ P^-_{W/\ell}(x) &= \frac{g^2}{32\pi^2 x}(1-x)^2\ln\left(\frac{4x^2E_\ell^2}{M_W^2}\right), \\ P^L_{W/\ell}(x) &= \frac{g^2}{16\pi^2 x}(1-x). \end{aligned} \tag{A2}$$

The matrix element of the subprocess $W^\mu(q_1)W^\nu(q_2) \to h(k_1)h(k_2)$ is

$$\begin{aligned} M^{\mu\nu} = &\left[\frac{3m_h^2 g_{hWW}}{(\hat{s}-m_h^2)v} + 2g_{hhWW} + \left(\frac{g_{hWW}^2}{\hat{t}-m_W^2} + \frac{g_{hWW}^2}{\hat{u}-m_W^2}\right)\right] g^{\mu\nu} \\ &- \frac{g_{hWW}^2}{m_W^2}\left[\frac{(q_1-k_1)^\mu(q_1-k_1)^\nu}{\hat{t}-m_W^2} + \frac{(q_1-k_2)^\mu(q_1-k_2)^\nu}{\hat{u}-m_W^2}\right], \end{aligned} \tag{A3}$$

where $\hat{s}$ ($\hat{t}$, $\hat{u}$) are Mandelstam variables of the subprocess, and g_{hWW} and g_{hhWW} are gauge couplings of the Higgs boson with $W^\pm$ boson. The SM presents the couplings in the following:

$$g^{\rm SM}_{hhWW} = \frac{m_W^2}{v^2}, \qquad g^{\rm SM}_{hWW} = 2\frac{m_W^2}{v}, \tag{A4}$$

where $v = 246$ GeV refers to the electroweak symmetry breaking scale. The couplings are parametrized as $g_{hWW} = \kappa_{hWW} g^{\rm SM}_{hWW}$ and $g_{hhWW} = \kappa_{hhWW} g^{\rm SM}_{hhWW}$. The cross section of the subprocess $W^+W^- \to hh$ can then be parametrized as follows:

$$\begin{aligned} \sigma(W^+W^- \to hh) = &\kappa^2_{hhWW}\sigma_a + \kappa^4_{hWW}\sigma_b + \kappa^2_{hWW}\sigma_c \\ &+ \kappa_{hhWW}\kappa^2_{hWW}\sigma_{ab} + \kappa_{hhWW}\kappa_{hWW}\sigma_{ac} \\ &+ \kappa^3_{hWW}\sigma_{bc}, \end{aligned} \tag{A5}$$

where σ_a, σ_b, and σ_c parametrize the contribution from Feynman diagrams (a), (b), and (c) depicted in Fig. 2, whereas σ_{ab}, σ_{ac}, and σ_{bc} are the corresponding interferential contributions. The cross section of the complete process, i.e., $\ell^-\ell^+ \to \nu_\ell\bar{\nu}_\ell hh$, can be parametrized similarly. The dependence of the cross section of $W^+W^- \to hh$ on the couplings κ_{hWW} and κ_{hhWW} can be inferred from the parameters in Eq. (A5). As shown in Fig. 8, the contributions from Feynman diagrams (a) and (b) in Fig. 7 and their corresponding interference components dominate the cross section.

In high-energy limits, the amplitude can be depicted by

$$\mathcal{M}_{LL} = M^{\mu\nu}\epsilon_L^\mu(q_1)\epsilon_L^\nu(q_2) = \frac{\hat{s}}{v^2}\left(\kappa_{hhWW} - \kappa^2_{hWW}\right) + \mathcal{O}(\hat{s}^0), \tag{A6}$$

for the longitudinally polarized vector bosons. This notion holds true as the longitudinal polarization vector $\epsilon_L^\mu(q)$ approximates to q^μ/m_W. This expression reveals that high energy collision regions primarily receive contributions from Feynman diagrams (a) and (b), a finding that is consistent with the above numeric result. Furthermore, the violation of the unitarity bound is inevitable unless the sum rule detailed below is fulfilled:

$$\kappa_{hhWW} - \kappa^2_{hWW} = 0. \tag{A7}$$

Perturbative unitarity requires the partial wave amplitude a_l [43,44] to satisfy

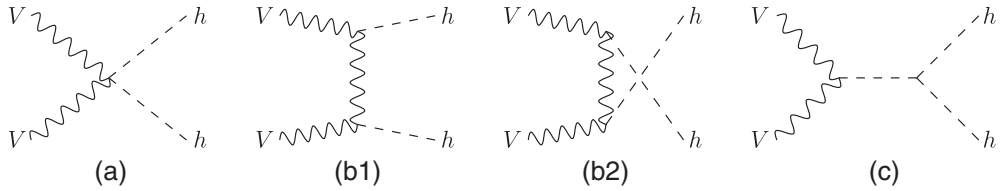

FIG. 7. Feynman diagrams representing $VV \to hh$ ($V = W^{\pm}/Z$) processes. These correspond to the factorized subprocess shown in Fig. 2.

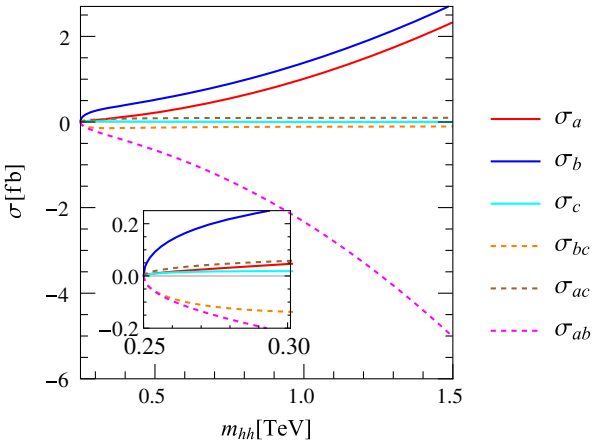

FIG. 8. The energy dependence of each Feynman diagram contribution of the subprocess $W_L^+W_L^- \to hh$. The solid line denotes the contribution from Feynman diagram (a),(b), and (c), respectively, and the dashed line the interference contribution.

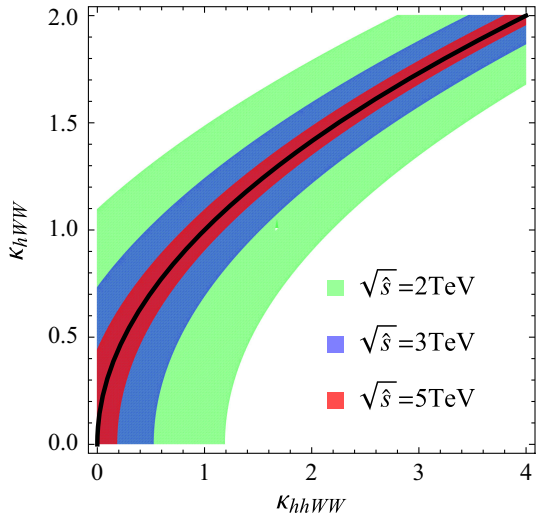

FIG. 9. Parameter space of κ_{hhWW} and κ_{hWW} that satisfies unitarity.

$$|\mathrm{Re}a_l| \leq 1/2, \tag{A8}$$

with the definition of

$$a_l = \frac{1}{32\pi}\int_{-1}^{1} \mathcal{M}(\hat{s},\hat{t})\mathrm{P}_l(\cos\theta)\, d\,\cos\theta, \tag{A9}$$

and $\mathcal{M}(\hat{s},\hat{t})$ is an amplitude of the process $W^-W^+ \to hh$ given in Eq. (A6). Consequently, the unitarity bound constrains the parameters κ_{hWW} and κ_{hhWW} for a given collision energy $\sqrt{\hat{s}}$ of the subprocess; see Fig. 9. The colored regions in the figure represent the unitarity-consistent areas for various collision energies, while the solid black line indicates the sum rule in Eq. (A7). The figure demonstrates that, as $\sqrt{\hat{s}} = m_{hh}$ increases, deviations from the sum rule must become less severe to maintain the theory consistence.

[1] G. Aad *et al.* (ATLAS Collaboration), Phys. Lett. B **716**, 1 (2012).
[2] S. Chatrchyan *et al.* (CMS Collaboration), Phys. Lett. B **716**, 30 (2012).
[3] K. Agashe, R. Contino, and A. Pomarol, Nucl. Phys. **B719**, 165 (2005).
[4] A. M. Sirunyan *et al.* (CMS Collaboration), Eur. Phys. J. C **79**, 421 (2019).
[5] P. Sharma and A. Shivaji, J. High Energy Phys. 10 (2022) 108.
[6] D. de Florian and J. Mazzitelli, Phys. Rev. Lett. **111**, 201801 (2013).
[7] G. Aad *et al.* (ATLAS Collaboration), J. High Energy Phys. 07 (2020) 108; 01 (2021) 145(E); 05 (2021) 207(E).
[8] G. Aad *et al.* (ATLAS Collaboration), Phys. Rev. D **108**, 052003 (2023).
[9] Anisha, O. Atkinson, A. Bhardwaj, C. Englert, and P. Stylianou, J. High Energy Phys. 10 (2022) 172.
[10] P. Roloff, U. Schnoor, R. Simoniello, and B. Xu (CLICdp Collaboration), Eur. Phys. J. C **80**, 1010 (2020).

[11] T. Han, D. Liu, I. Low, and X. Wang, Phys. Rev. D **103**, 013002 (2021).
[12] M. Gonzalez-Lopez, M. J. Herrero, and P. Martinez-Suarez, Eur. Phys. J. C **81**, 260 (2021).
[13] T. Han, Y. Ma, and K. Xie, Phys. Rev. D **103**, L031301 (2021).
[14] M. Lu, A. M. Levin, C. Li, A. Agapitos, Q. Li, F. Meng, S. Qian, J. Xiao, and T. Yang, Adv. High Energy Phys. **2021**, 6693618 (2021).
[15] C. Accettura *et al.*, Eur. Phys. J. C **83**, 864 (2023).
[16] H. Baer *et al.* (ILC Collaboration), arXiv:1306.6352.
[17] D. M. Asner *et al.*, in Community summer study 2013: Snowmass on the Mississippi (2013), arXiv:1310.0763.
[18] M. Dong *et al.* (CEPC Study Group Collaboration), arXiv:1811.10545.
[19] A. Aryshev *et al.* (ILC International Development Team Collaboration), arXiv:2203.07622.
[20] G. I. Budker, Conf. Proc. C **690827**, 33 (1969).
[21] V. V. Parkhomchuk and A. N. Skrinsky, Conf. Proc. C **830811**, 485 (1983).
[22] D. Neuffer, Part. Accel. **14**, 75 (1983).
[23] R. Palmer *et al.*, Nucl. Phys. B, Proc. Suppl. **51**, 61 (1996).
[24] D. Stratakis *et al.*, arXiv:2203.08033.
[25] B. Abbott *et al.*, Phys. Rev. D **108**, 093009 (2023).
[26] C. Aimè *et al.*, in 2022 Snowmass summer study (2022), arXiv:2203.07256.
[27] T. Han, Z. Liu, L.-T. Wang, and X. Wang, in 2022 Snowmass summer study (2022), arXiv:2203.07351.
[28] T. Han, T. Li, and X. Wang, in 2022 Snowmass summer study (2022), arXiv:2203.05484.
[29] J. P. Delahaye, M. Diemoz, K. Long, B. Mansoulié, N. Pastrone, L. Rivkin, D. Schulte, A. Skrinsky, and A. Wulzer, arXiv:1901.06150.
[30] K. Long, D. Lucchesi, M. Palmer, N. Pastrone, D. Schulte, and V. Shiltsev, Nat. Phys. **17**, 289 (2021).
[31] J. Alwall, R. Frederix, S. Frixione, V. Hirschi, F. Maltoni, O. Mattelaer, H. S. Shao, T. Stelzer, P. Torrielli, and M. Zaro, J. High Energy Phys. 07 (2014) 079.
[32] T. Sjostrand, S. Mrenna, and P. Z. Skands, Comput. Phys. Commun. **178**, 852 (2008).
[33] M. Cacciari, G. P. Salam, and G. Soyez, Eur. Phys. J. C **72**, 1896 (2012).
[34] J. de Favereau, C. Delaere, P. Demin, A. Giammanco, V. Lemaître, A. Mertens, and M. Selvaggi (DELPHES 3 Collaboration), J. High Energy Phys. 02 (2014) 057.
[35] G. W.-S. Hou, Nucl. Phys. B, Proc. Suppl. **51**, 40 (1996).
[36] S. Y. Choi, C. S. Kim, Y. J. Kwon, and S.-H. Lee, Phys. Rev. D **57**, 7023 (1998).
[37] V. D. Barger, S. Pakvasa, and X. Tata, Phys. Lett. B **415**, 200 (1997).
[38] J. M. Dávila, D. Domenech, M. J. Herrero, and R. A. Morales, arXiv:2312.03877.
[39] A. Costantini, F. De Lillo, F. Maltoni, L. Mantani, O. Mattelaer, R. Ruiz, and X. Zhao, J. High Energy Phys. 09 (2020) 080.
[40] R. Ruiz, A. Costantini, F. Maltoni, and O. Mattelaer, J. High Energy Phys. 06 (2022) 114.
[41] S. Dawson, Nucl. Phys. **B249**, 42 (1985).
[42] V. D. Barger, K.-m. Cheung, T. Han, and R. J. N. Phillips, Phys. Rev. D **42**, 3052 (1990).
[43] B. W. Lee, C. Quigg, and H. B. Thacker, Phys. Rev. Lett. **38**, 883 (1977).
[44] B. W. Lee, C. Quigg, and H. B. Thacker, Phys. Rev. D **16**, 1519 (1977).